Supporting Information:

Highly negative Poisson's ratio in thermally conductive covalent organic frameworks

Ashutosh Giri,[1, a)] Austin M. Evans,[1] Muhammad Akif Rahman,[2] Alan J. H. McGaughey,[3] and Patrick E. Hopkins[4, 5, 6, b)]

[1)]*Department of Chemistry and Applied Physics, Columbia University, New York City, NY 10027, USA*

[2)]*Department of Mechanical, Industrial and Systems Engineering, University of Rhode Island, Kingston, RI 02881, USA*

[3)]*Department of Mechanical Engineering, Carnegie Mellon University, Pittsburgh, PA 15213, USA*

[4)]*Department of Mechanical and Aerospace Engineering, University of Virginia, Charlottesville, Virginia 22904, USA*

[5)]*Department of Materials Science and Engineering, University of Virginia, Charlottesville, Virginia 22904, USA*

[6)]*Department of Physics, University of Virginia, Charlottesville, Virginia 22904, USA*

[a)]Electronic mail: ashgiri@uri.edu

[b)]Electronic mail: phopkins@virginia.edu

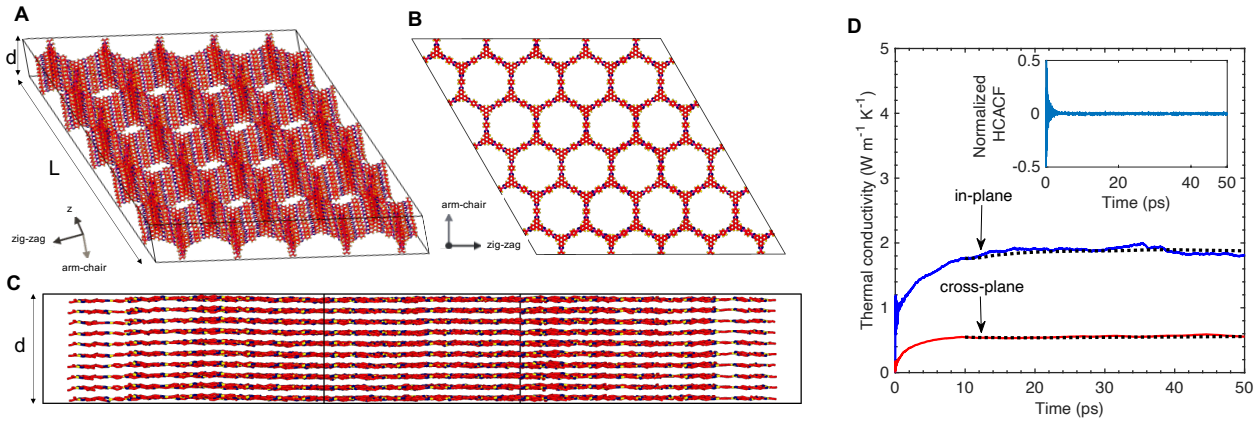

Figure S1. (a) Three-dimensional view of the computational domain of our COF-5 structure used for our molecular dynamics simulations. (b) Top view and (c) side view of the schematic of the COF-5 structure. The thickness d and the length L are varied in the simulations to obtain (size-independent) converged results. (d) Converged values of in-plane and cross-plane thermal conductivities obtained for our COF-5 structure from the integral of the heat current autocorrelation function (HCACF). (inset) Normalized HCACF vs time for our COF-5 structure which shows that the HCACF decays to zero within the first 10 ps.

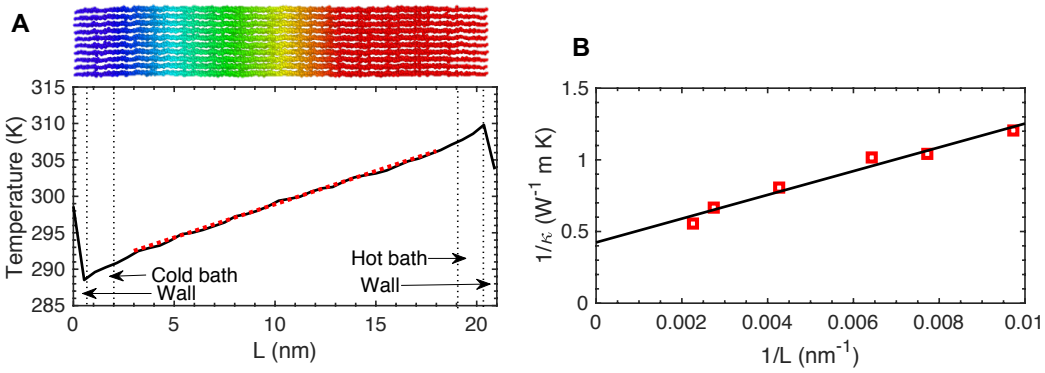

Figure S2. (a) Temperature profile in the in-plane direction for COF-5 in our non-equilibrium molecular dynamics (NEMD) simulations. (b) . NEMD-predicted inverse of size-dependent thermal conductivities as a function of the inverse of computational domain length in the applied heat flux direction for our COF-5 structure. The linear dependence of MD results suggests that pronounced size effects are observed for the COFs in the in-plane direction. The extrapolation to $1/d \rightarrow 0$ predicts the thermal conductivity of an infinite system with the assumption that the minimum system size used in these NEMD simulations is comparable to or larger than the largest mean-free-paths of heat carrying vibrations in the in-plane direction for the COF-5 structures.

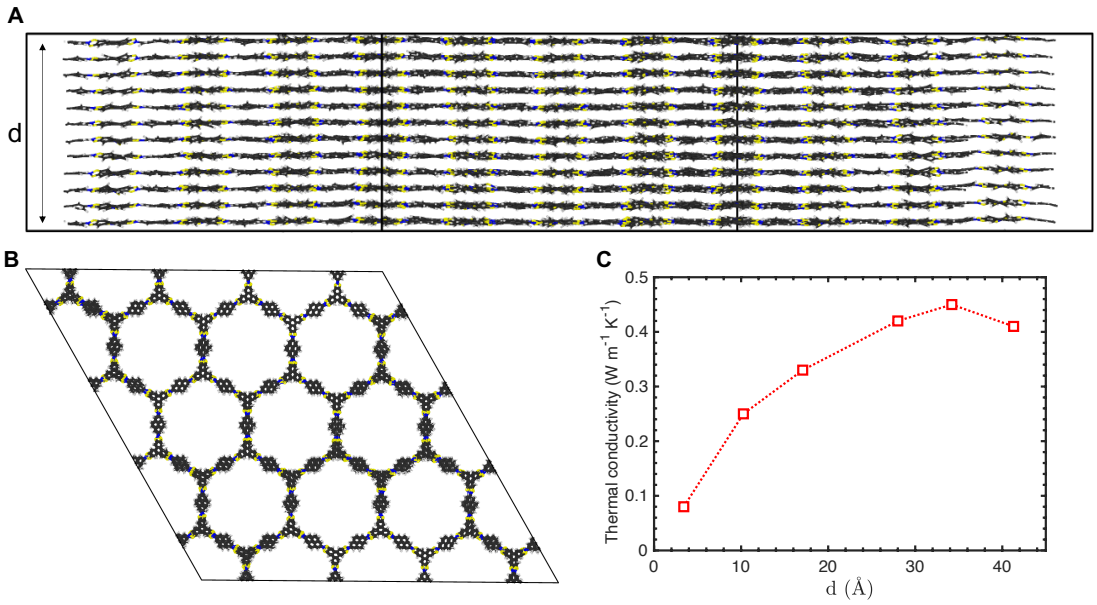

Figure S3. Schematic of the computational domain for TP-COF as viewed along the (a) z-axis and (b) $zz - ac$ plane. (c) Cross-plane thermal conductivity of TP-COF predicted via the Green Kubo approach as a function of thickness, (d).

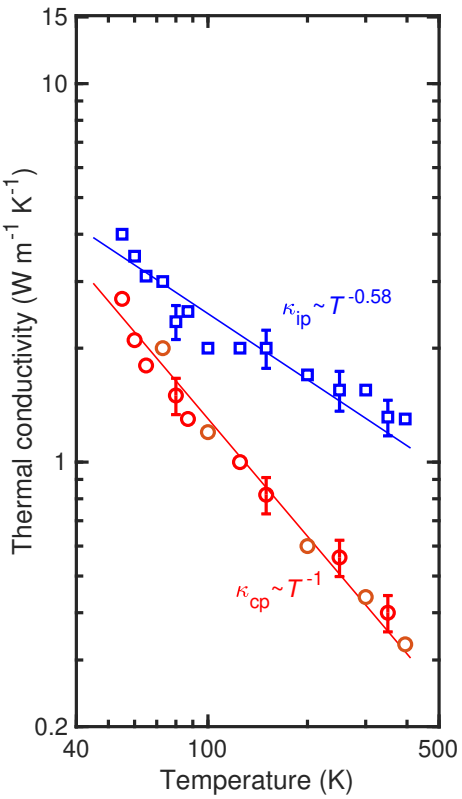

Figure S4. Temperature dependent thermal conductivity of TP-COF. The cross-plane thermal conductivity has a larger temperature dependence as shown by the $\sim T^{-1}$ trend.

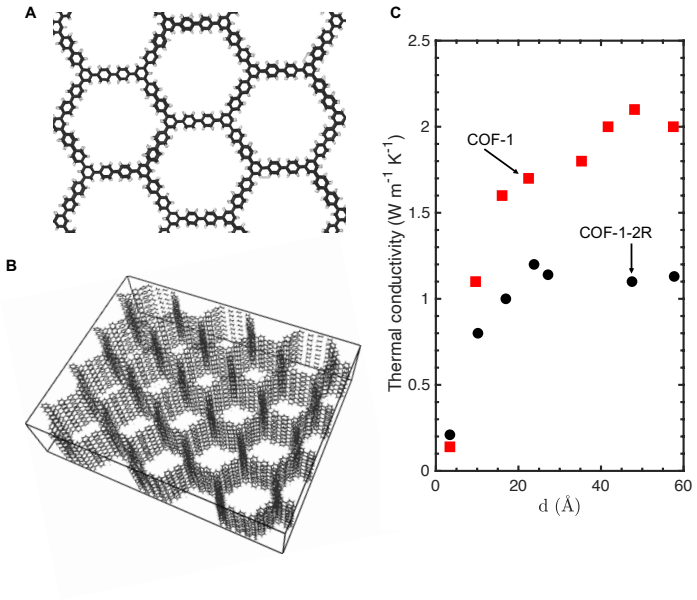

Figure S5. Schematics of the computational domain for COF-1-2R structure along the (a) $zz - ac$ plane and (b) the full perspective view. (c) Cross-plane thermal conductivities of COF-1-2R and COF-1 predicted via the Green Kubo approach as a function of thickness, (d).

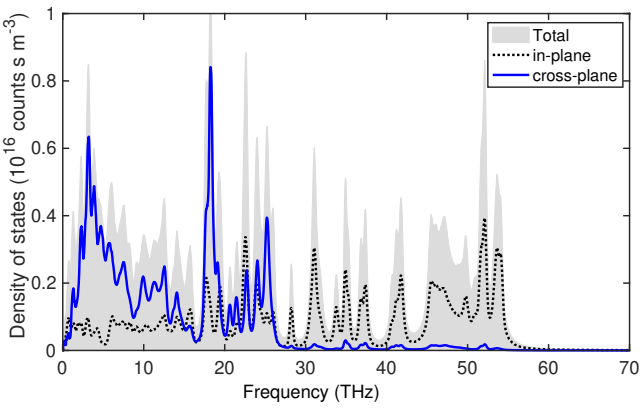

Figure S6. MD-predicted vibrational density of states for COF-5.

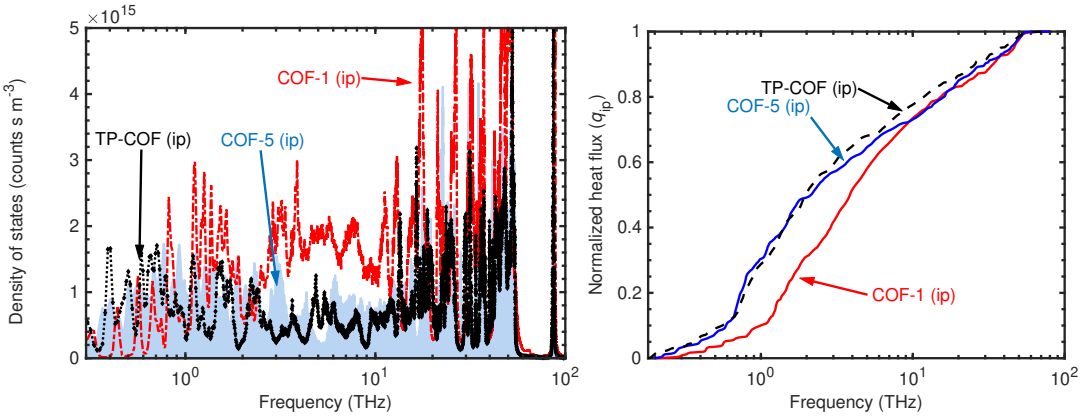

Figure S7. (a) Comparison of MD-predicted vibrational density of states for COF-1, COF-5 and TP-COF in the in-plane direction. (b) Normalized heat flux accumulation versus frequency for the three structures in the in-plane direction. While the spectral heat flux are almost identical for the lesser dense COF-5 and TP-COF structures, the higher frequency modes in the COF-1 structure have a comparatively larger contribution to heat conduction.

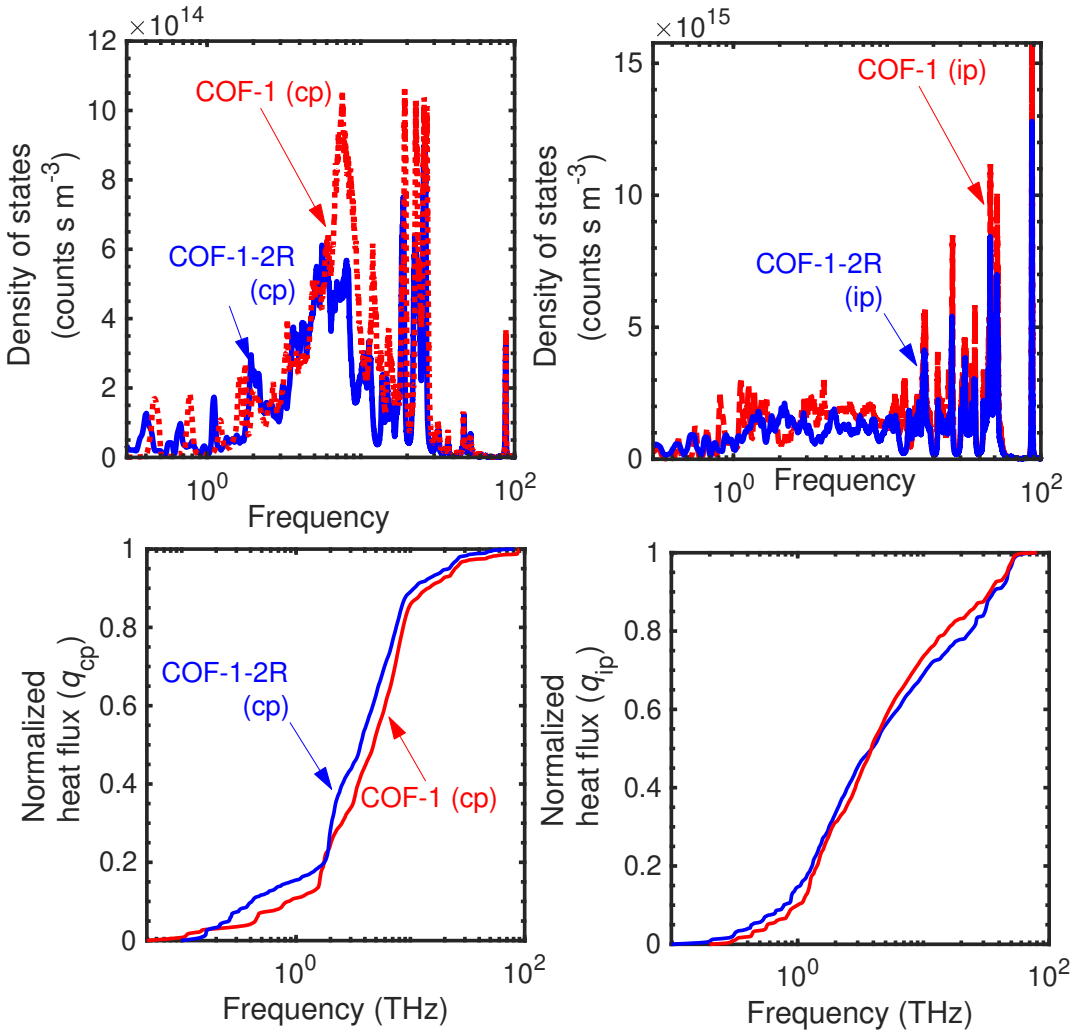

Figure S8. MD-predicted vibrational density of states for COF-1 and COF-1-2R in the (a) cross-plane and (b) in-plane direction. Normalized heat flux accumulation versus frequency in the (c) cross-plane and (d) in-plane directions for the two structures showing very similar trends in the spectral heat flux.

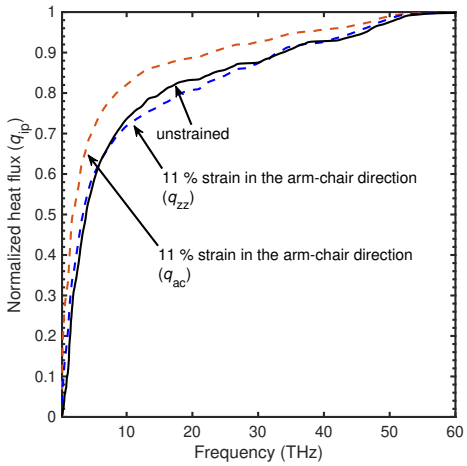

Figure S9. Comparison between the normalized heat flux accumulation versus frequency in the in-plane direction for an unstrained and strained COF-1 structures. The uniaxial strain is applied in the arm-chair direction, which results in a shift of heat carrying vibrations to lower frequencies in this direction.

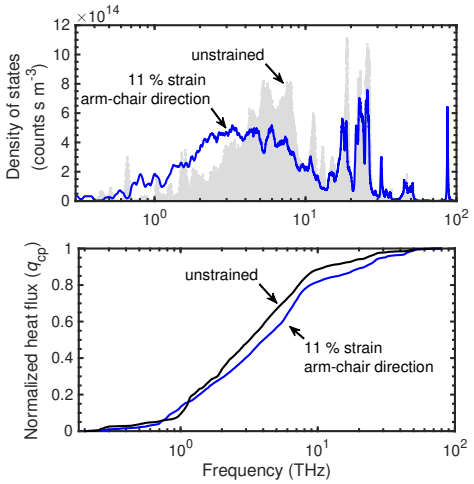

Figure S10. (a) MD-predicted vibrational density of states for unstrained and uniaxially strained COF-1 in the cross plane direction. (b) Normalized heat flux accumulation in the cross-plane direction for the unstrained and strained structure.

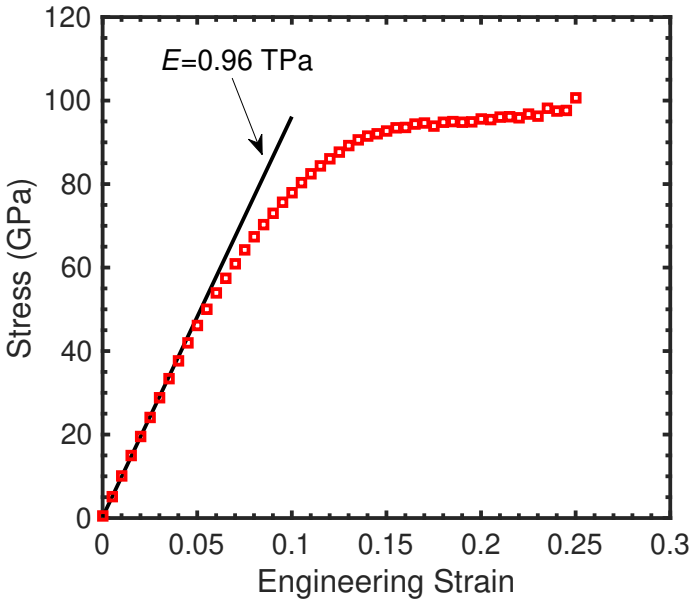

Figure S11. Stress-strain curve for graphite showing the Young's modulus predicted from the initial elastic response.

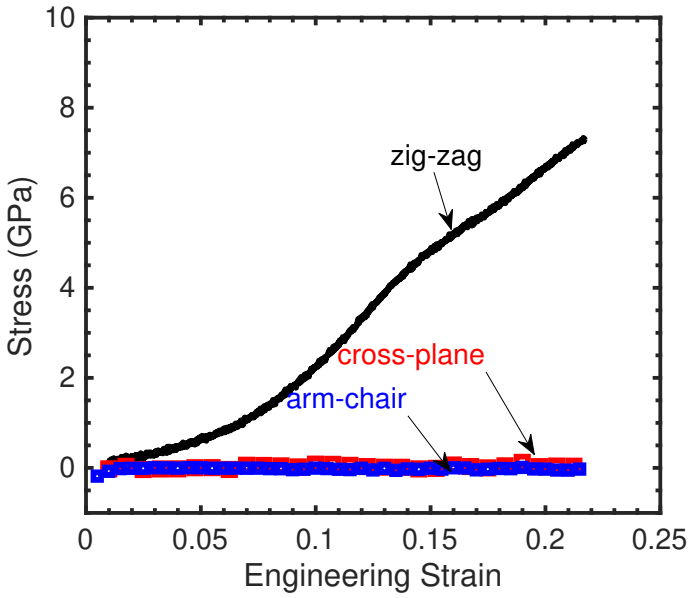

Figure S12. Stress-strain curve for COF-5 calculated under uniaxial tension along the zig-zag direction. The other two directions are "stress-free" during the tensile simulations.

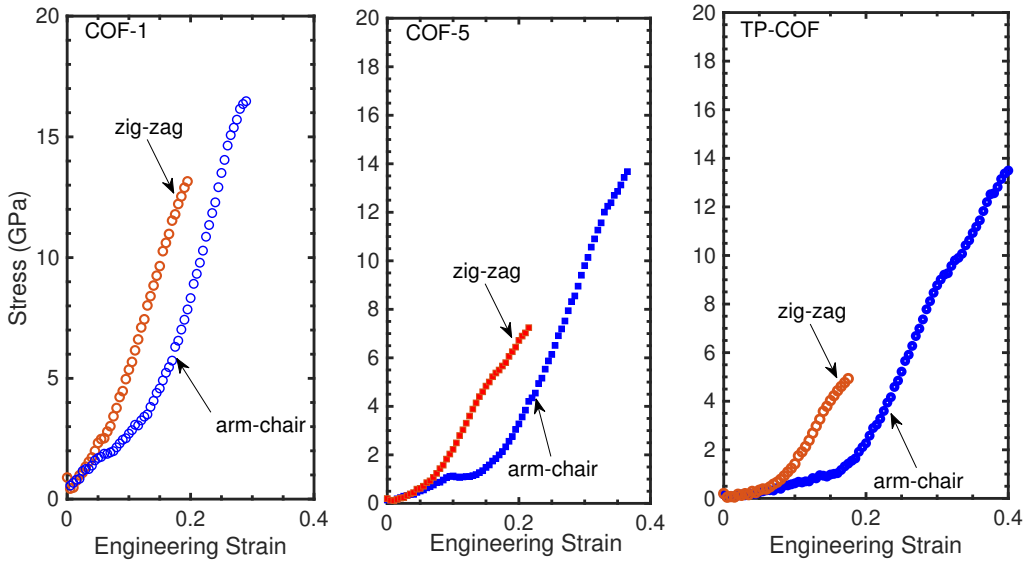

Figure S13. Stress-strain curve for (a) COF-1, (b) COF-5 and (c) TP-COF calculated under uniaxial tension along the zig-zag or arm-chair directions.

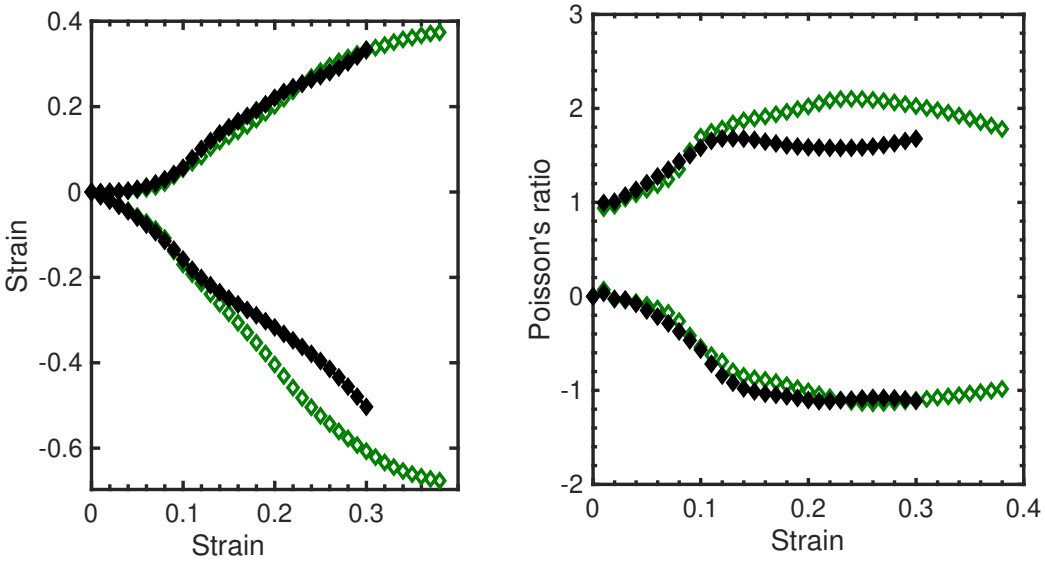

Figure S14. (a) Induced strains in the orthogonal directions as a function of strain in the arm-chair (hollow symbols) and zig-zag (solid symbols) directions for our COF-5 structure. (b) The resulting poisson's ratio as a function of the applied uniaxial strain.

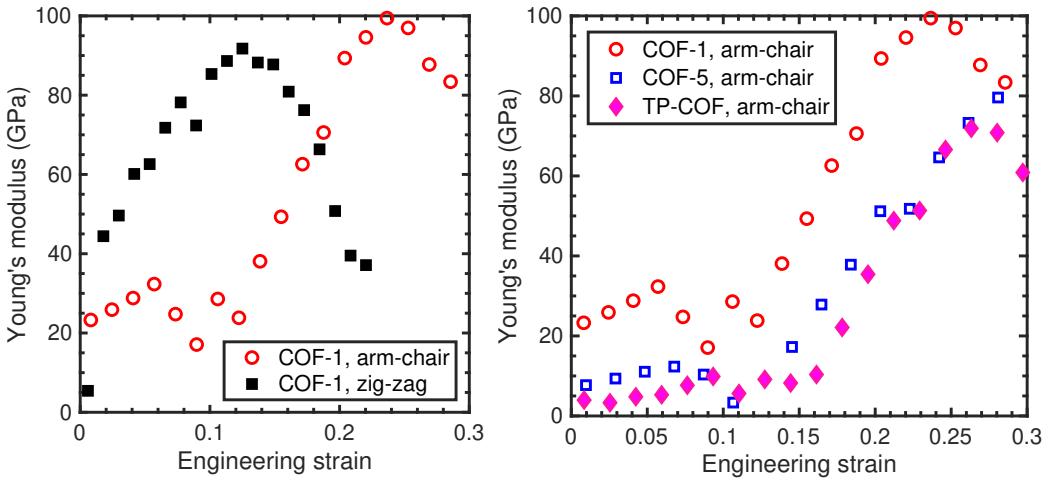

Figure S15. Young's modulus as a function of applied strain in the arm-chair (hollow symbols) and zig-zag (solid symbols) for our COF-1 structure. (b) Comparison of Young's modulii as a function of applied strain in the arm-chair direction for COF-1, COF-5 and TP-COF.

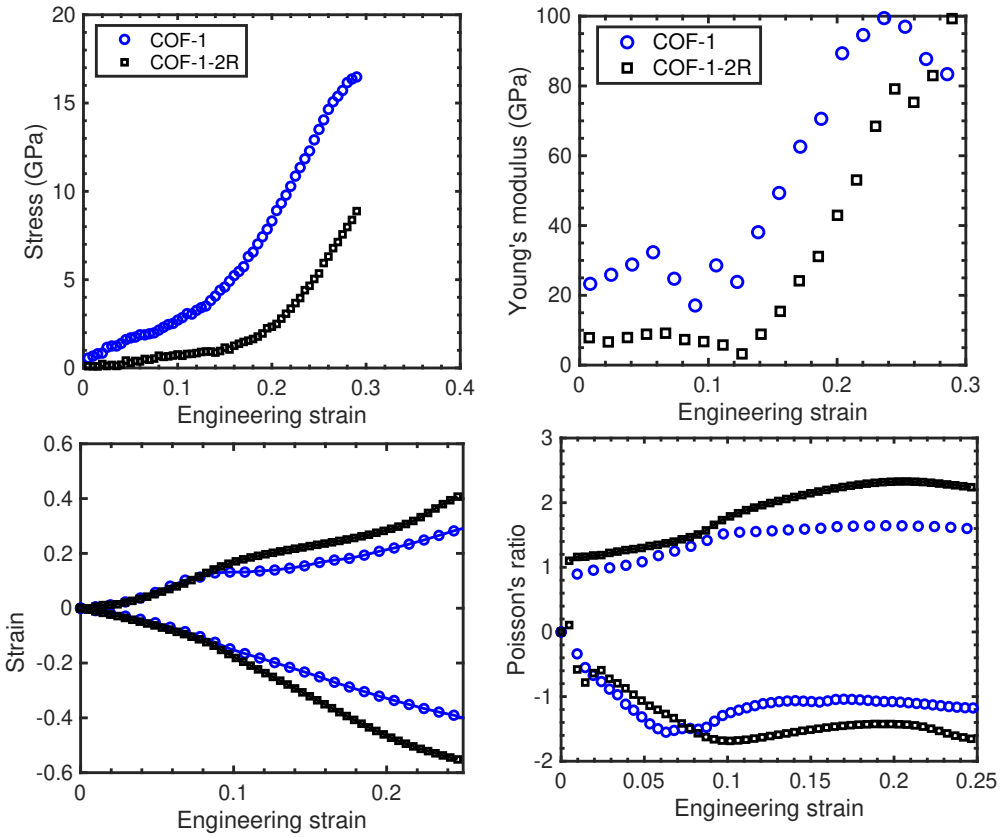

Figure S16. Comparison between the mechanical responses of COF-1 and COF-1-2R structures. (a) Stress-strain curve as a function of uniaxial strain in the arm-chair direction. (b) Young's modulus as a function of applied strain in the arm-chair. (c) Induced strains in the orthogonal directions as a function of strain in the arm-chair. (d) Poisson's ratio in the zig-zag and cross-plane directions.

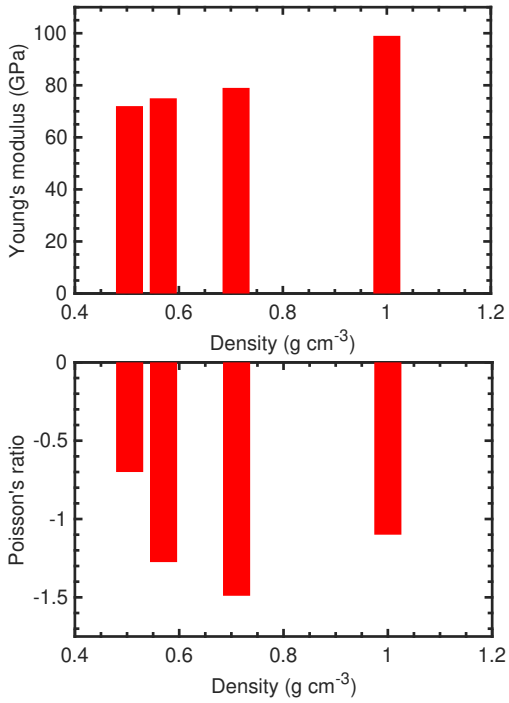

Figure S17. (a) Young's modulus as a function of density for the four COFs at 20 % strain in the arm-chair direction showing a monotonic increase. (b) Poisson's ratio as a function of density at 20 % applied strain .

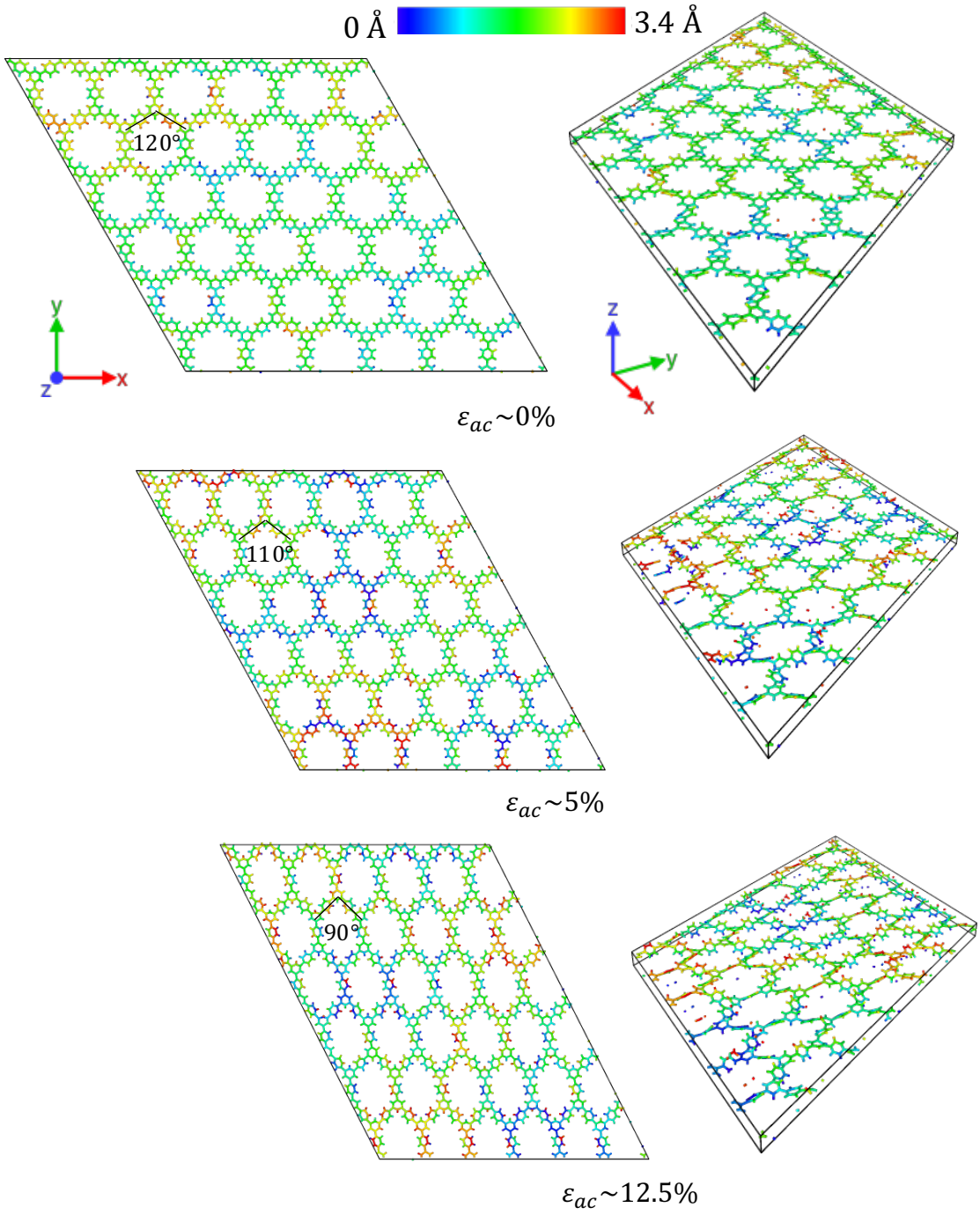

Figure S18. Snapshots of the COF-1 structure at various strain levels showing atoms and bonds colored according to their z-coordinate.

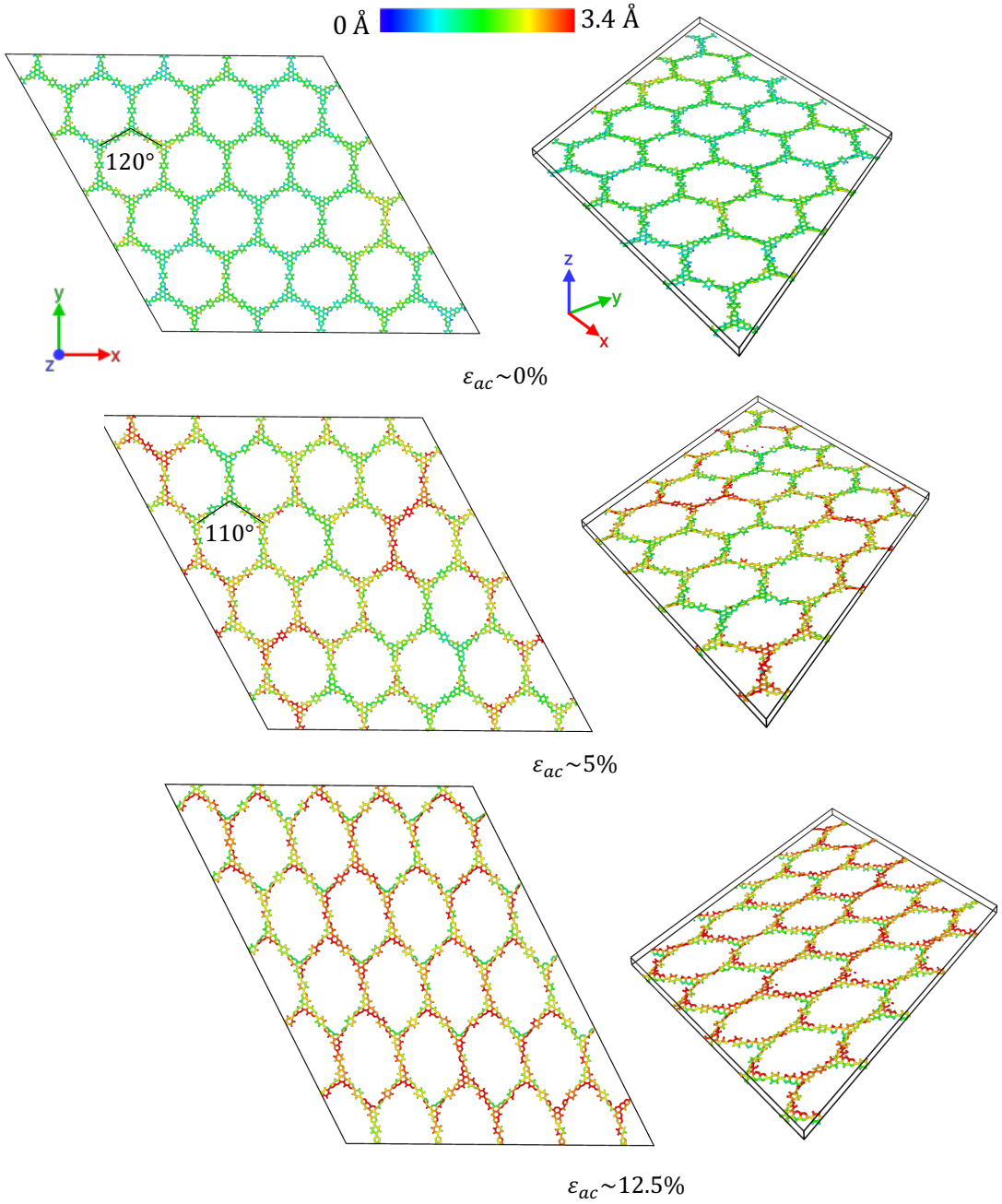

Figure S19. Snapshots of the COF-5 structure at various strain levels showing atoms and bonds colored according to their z-coordinate.

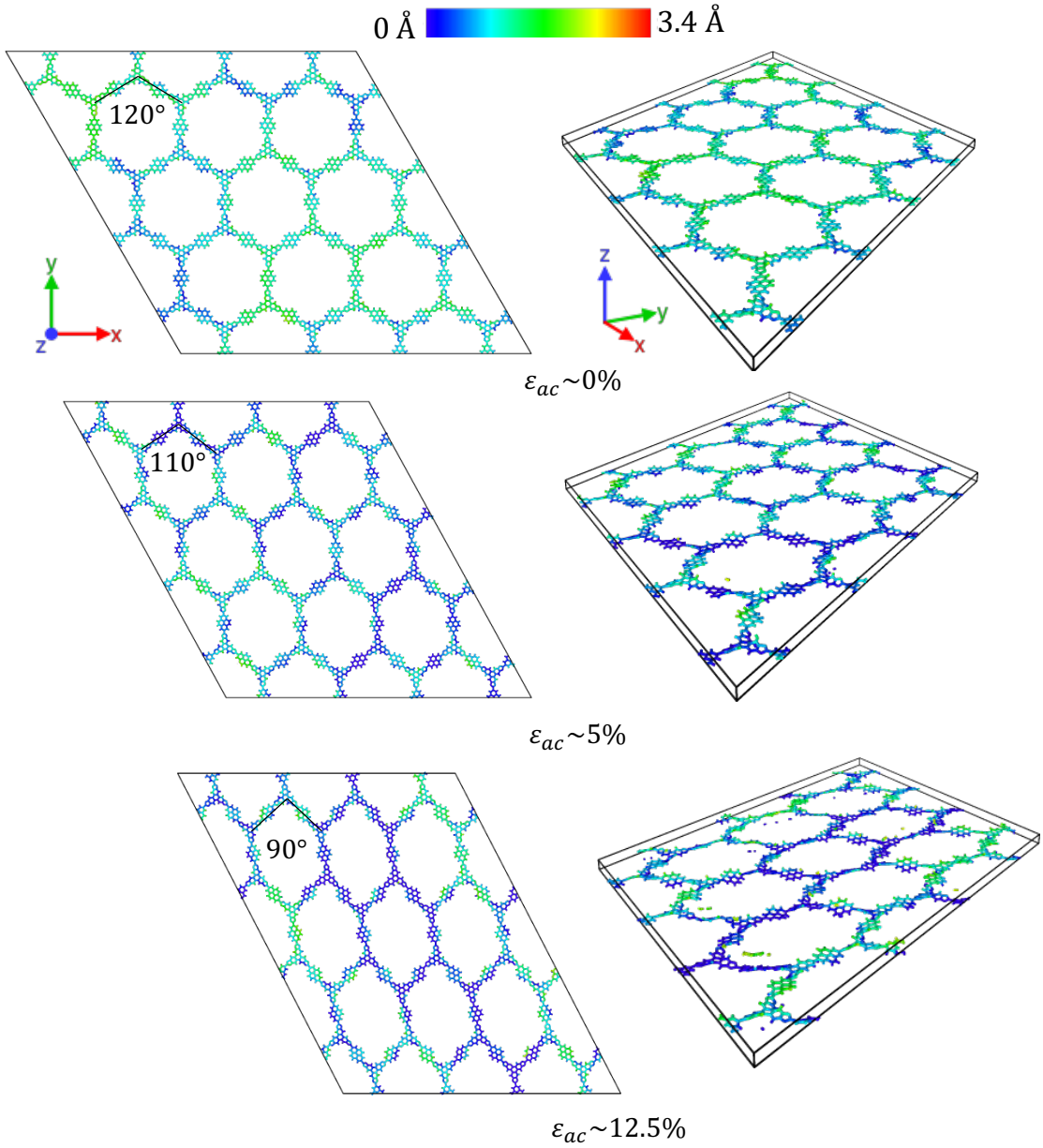

Figure S20. Snapshots of the TP-COF structure at various strain levels showing atoms and bonds colored according to their z-coordinate.

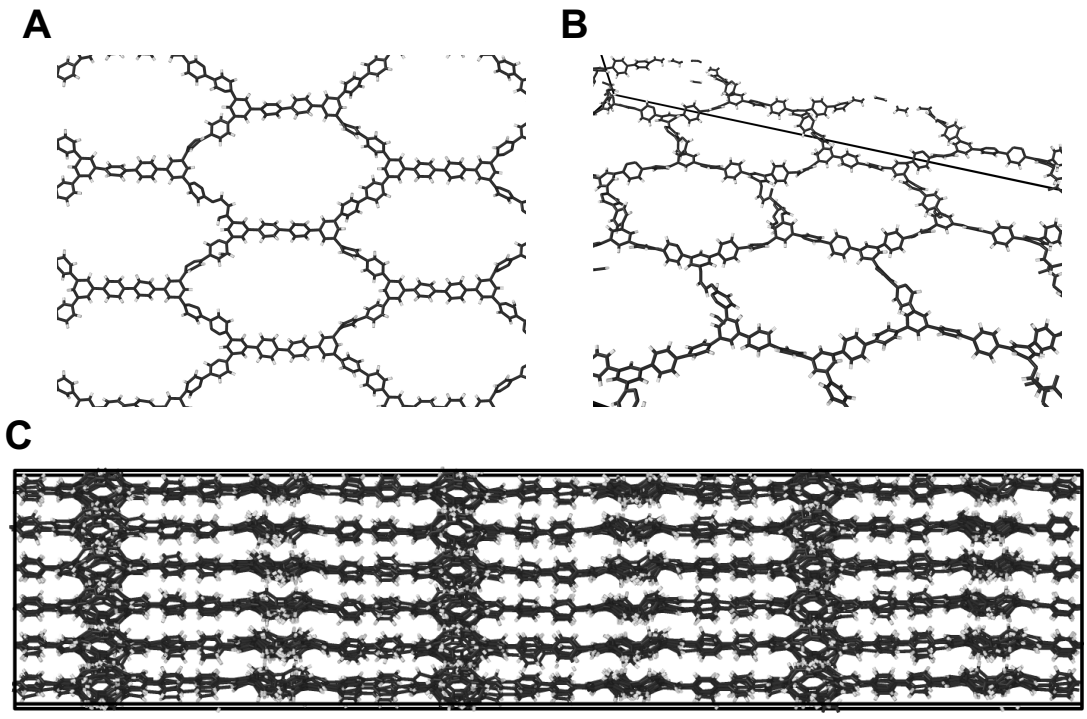

Figure S21. Snapshots of the COF-1-2R structure at 10 % strain showing the orientational change of the phenyl rings (from near planar positions) due to uniaxial strain in the arm-chair direction.

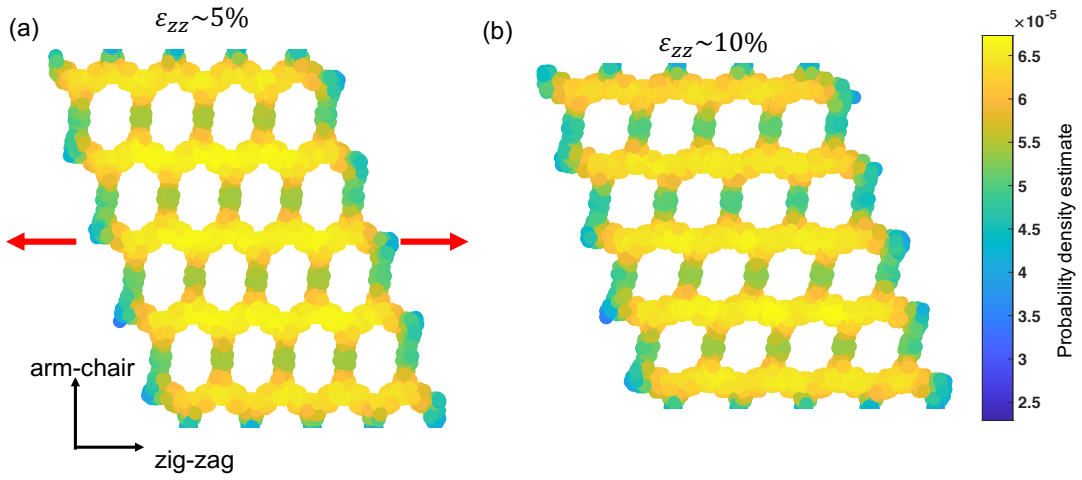

Figure S22. Snapshots of the COF-5 structure at (a) 5% and (b) 10% strain showing the probability density estimate of atomic positions relative to the zz-ac plane. As the tensile strain increases, the swiveling and rotational motion of the aromatic rings along the arm-chair direction is quantified by the lower probability density estimate, whereas, the better orientation of the polymer building blocks along the direction of the tensile axis is demonstrated by the relatively higher probability density estimate of atoms along the zig-zag direction.

Although the GK approach has been extensively used to predict thermal conductivity of different material systems,[1–9] there has been considerable amount of work in literature showing the accurate calculation of the thermal conductivity via Eq. 1 due to uncertainties associated with finite simulation times and domain sizes.[2,4,7,10–14] To ensure that the EMD-predicted thermal conductivities are not influenced by size effects, the dimensions of the simulation box are chosen to produce converged values of thermal conductivities. To this end, the thermal conductivities of structures with cross-sections of 15×13 nm^2 and 30×26 nm^2 are comparable within uncertainties. Similarly, the thermal conductivities of structures with computational domain sizes of $15.1\times13.1\times3.4$ nm^3, and $15.1\times13.1\times10.2$ nm^3 are also similar within uncertainties.

Recently, the use of the heat current calculations in LAMMPS has been shown to predict erroneous thermal conductivities for structures with mandy-body interatomic potentials.[15,16] Therefore, to gain confidence in our GK calculations, we run additional nonequilibrium MD (NEMD) simulations for our COF-5 structures. We add a fixed amount of energy per time step (0.4 eV ps^{-1}) to a heat bath at one end of the computational domain and remove an equal amount of energy from a cold bath at the other end to establish a steady-state temperature gradient across the in-plane direction of our COF-5 structures. Note, these simulations are performed under the microcanonical ensemble (NVE integration) where the number of atoms (N), volume (V), and energy (E) of the system are held constant. A fixed wall at either side in the in-plane direction is enforced. The temperature of the atoms are averaged along equally spaced bins in the applied heat flux direction for a total of 10 ns to produce the temperature profiles as shown in Fig. S2a. Fourier's law is invoked to calculate the thermal conductivity of our simulation domains. As the fixed walls can scatter the long wavelength phonons, we calculate thermal conductivities for different domain lengths to accurately predict the bulk in-plane thermal conductivity of our COF-5 structure in the in-plane direction. Extrapolating the inverse of thermal conductivity, $1/\kappa$, to the inverse of the computational domain length, $1/d$=0, as shown in Fig. S2b, allows us to predict the size-independent in-plane thermal conductivity of $\sim$2.3 W m^{-1} K^{-1} for our COF-5 system, which is similar to our GK prediction.[17]

Figure S3 shows the schematic of the computational domain and the GK-predicted thermal conductivity as a function of thickness in the cross-plane direction for our TP-COF structures. The cross-plane thermal conductivity is similar beyond $d\sim$3.5 nm confirming no size-effects are influencing our results for the TP-COF structures. Figure S4 shows the temperature dependent thermal conductivity of TP-COF domains showing the Umklapp dominated thermal conductivity

in the cross-plane directions for these materials.

Figure S5a-b show the schematics of the COF-1-2R computational domains made by adding a phenyl ring to the COF-1 structures. Thermal conductivities as a function of thicknesses in the cross-plane directions for COF-1 and COF-1-2R shows that $d>$ 4nm is enough to ensure no size-effects are influencing our results.

We calculate the vibrational density of states (DOS) from our MD simulations. The velocities of the atoms in the COF-5 structure are output every 10 time steps for a total of 1 ns. A velocity autocorrelation function algorithm is used to obtain the local phonon DOS in the cross-plane and in-plane directions as shown in Fig. S6. The density of states, $D(\omega)$, is obtained from the fourier transform ($\mathcal{F}$) of the velocity correlation function (VACF).[1] The Welch method of power spectral density estimation is applied to obtain the $D(\omega)$ and is normalized as follows,

$$D(\omega) = \frac{1}{2} m \mathcal{F}(VACF) \frac{1}{k_{\mathrm{B}} T} \rho \tag{1}$$

where m is the atomic mass, k_{B} is the Boltzmann constant, T is the local temperature, and ρ is the atomic density.

We base the spectral heat flux calculations on the analysis as detailed in our previous work in Ref. 18. Briefly, the heat current between atoms i and j is proportional to the correlation between the force, $\overrightarrow{F_{ij}}$, and the velocities, $\vec{v}$, of the two atoms and is given as, $q_{i\rightarrow j}(\omega) \propto \left\langle \overrightarrow{F_{ij}} \cdot (\vec{v_i} + \vec{v_j}) \right\rangle$, where $\langle\rangle$ denotes a steady-state nonequilibrium ensemble average.[18–20] We tabulate the forces and velocities of a group of atoms for a total of 2 ns with 5 fs time intervals under the NVE ensemble to calculate the spectral heat fluxes along both the in-plane and cross-plane directions. Following this approach, the normalized heat flux as a function of frequency in the in-plane directions for our COF-1, COF-5 and TP-COF structures are shown in Fig. S7b. Although the DOS for these structures appear to be similar for the entire vibrational spectrum (see Fig. S7a), we find that higher frequencies (in the 1 to 10 THz range) are more responsible for heat conduction in the COF-1 structure. We also compare the DOS and spectral heat flux calculations for our COF-1-2R structures with that of the COF-1 structure in Fig. S8.

The application of strain in the arm-chair direction is shown to drastically modify heat conduction in the direction of the applied strain (by shifting the heat carrying vibrations to lower frequencies; see Fig. S9). Whereas, the heat current accumulation remains the same for the zig-zag direction. Tensile strain is shown to soften the frequencies in the cross-plane direction as exemplified by the DOS calculations in the cross-plane direction for the COF-1 structure (see

Fig. S10a).

From our uniaxial tensile loading simulations, we predict a Young's modulus of $\sim$0.96 TPa for graphite (see Fig. S11), which is in excellent agreement with previous results.[21] In Fig. S12, we plot the stress-strain curve for COF-5 calculated under uniaxial tension along the zig-zag direction. The other two directions are "stress-free" during the tensile simulations through the application of an isobaric-isothermal ensemble for these directions, where the length of the simulation domain is allowed to relax. Figure S13 shows the stress-strain relationships for COF-1, COF-5 and TP-COF structures in the zig-zag and arm-chair directions. The structures are more mechanically stable when tensile force is applied in the arm-chair direction, whereas, the failure strain is lower in the zig-zag direction. For comparison of the induced strains in the orthogonal directions as a function of strain in the arm-chair and zig-zag directions, we plot the strain for our COF-5 structure in Fig. S14a. The application of tensile loading in the two directions have similar strain responses as also exemplified by the resulting poisson's ratio as a function of the applied uniaxial strain as shown in Fig. S14b.

The nonlinear stress-strain relationship for these 2D COF structures manifest in varying Young's moduli as a function of tensile strain as shown in Fig. S15a for COF-1 when pulled along the arm-chair and zig-zag directions. Figure S15b shows a comparison between the three COF structures showing the impact of mass density on the calculated Young's modulus of these materials. To observe the effect of mass density on the mechanical response to tensile loading, we compare the results for COF-1 and COF-1-2R structures in Fig. S16. Although the Young's modulus is higher for COF-1 with the higher mass density, the strain response is larger for COF-1-2R possibly due to the more number of phenyl groups that swivel in the structures. A comparison of the calculated Young's modulus and Poisson's ratio between the various structures as a function of mass density is also shown in FIg. S17.

The out of plane motion of atoms in the COF-1, COF-5 and TP-COF structures due to the application of tensile strain is shown in the schematics in Fig. S18, Fig. S19 and Fig. S20, respectively. The atoms are colored according to their positions relative to the z-axis. For all structures, the application of tensile strain is shown to perturb the z-axis positions of the atoms due to the swiveling motion of the phenyl rings. As shown by the color intensity, the phenyl rings in the COF-1 structure lead to the larger change in the z-axis positions of the atoms, thus leading to a comparatively higher negative Poisson's ratio. The swiveling motion in amplified in the COF-1-2R structure with 2 phenyl rings (as opposed to 1 phenyl ring in the COF-1 structure), which leads

to greater strain response in COF-1-2R.

In order to quantify the chain rotation upon applied strain, we calculate the probability density estimate for an atom's position with respect the plane defined by the $ac - zz$ plane. As such, the probability density estimate of an atom provides a quantitative measure of finding that atom in the specific plane. Therefore a higher value (yellow) indicates better overlap of atoms when projected onto the plane and evidently better orientation of the polymer chain along that direction. As the strain is increased from 5% to 10% (Fig. S22), the greater rotation of the aromatic rings with respect to the equilibrium plane leads to lower values (blue) for molecules along the arm-chair direction, whereas, molecules along the zig-zag direction have higher probability density estimates suggesting better orientational order along the direction of the applied strain.

REFERENCES

[1]M. P. Allen and D. J. Tildesley, *Computer simulation of liquids (Oxford Science Publications)*, reprint ed., Oxford science publications (Oxford University Press, 1989).

[2]P. K. Schelling, S. R. Phillpot, and P. Keblinski, Phys. Rev. B **65**, 144306 (2002).

[3]A. McGaughey and M. Kaviany, International Journal of Heat and Mass Transfer **47**, 1799 (2004).

[4]A. McGaughey and M. Kaviany, International Journal of Heat and Mass Transfer **47**, 1783 (2004).

[5]A. Henry and G. Chen, Phys. Rev. Lett. **101**, 235502 (2008).

[6]A. S. Henry and G. Chen, Journal of Computational and Theoretical Nanoscience **5**, 141 (2008).

[7]Z. Wang, S. Safarkhani, G. Lin, and X. Ruan, International Journal of Heat and Mass Transfer **112**, 267 (2017).

[8]W. Lv and A. Henry, New Journal of Physics **18**, 013028 (2016).

[9]Y. Chalopin, K. Esfarjani, A. Henry, S. Volz, and G. Chen, Phys. Rev. B **85**, 195302 (2012).

[10]J. Che, T. Çağın, W. Deng, and W. A. G. III, The Journal of Chemical Physics **113**, 6888 (2000), http://dx.doi.org/10.1063/1.1310223.

[11]J. Chen, G. Zhang, and B. Li, Physics Letters A **374**, 2392 (2010).

[12]S. G. Volz and G. Chen, Phys. Rev. B **61**, 2651 (2000).

[13]H. Dong, Z. Fan, L. Shi, A. Harju, and T. Ala-Nissila, Phys. Rev. B **97**, 094305 (2018).

[14]L. Sun and J. Y. Murthy, Applied Physics Letters **89**, 171919 (2006),

https://doi.org/10.1063/1.2364062.

[15]Z. Fan, L. F. C. Pereira, H.-Q. Wang, J.-C. Zheng, D. Donadio, and A. Harju, Phys. Rev. B **92**, 094301 (2015).

[16]P. Boone, H. Babaei, and C. E. Wilmer, *Journal of Chemical Theory and Computation*, Journal of Chemical Theory and Computation **15**, 5579 (2019).

[17]D. P. Sellan, E. S. Landry, J. E. Turney, A. J. H. McGaughey, and C. H. Amon, Phys. Rev. B **81**, 214305 (2010).

[18]A. Giri, J. L. Braun, and P. E. Hopkins, The Journal of Physical Chemistry C **120**, 24847 (2016).

[19]K. Sääskilahti, J. Oksanen, J. Tulkki, and S. Volz, Phys. Rev. B **90**, 134312 (2014).

[20]K. Sääskilahti, J. Oksanen, S. Volz, and J. Tulkki, Phys. Rev. B **91**, 115426 (2015).

[21]C. Lee, X. Wei, J. W. Kysar, and J. Hone, Science **321**, 385 (2008), http://science.sciencemag.org/content/321/5887/385.full.pdf.